Science Advances
AAAS

Supplementary Materials for

Membraneless organelles formed by liquid-liquid phase separation increase bacterial fitness

Xin Jin, Ji-Eun Lee, Charley Schaefer, Xinwei Luo, Adam J. M. Wollman, Alex L. Payne-Dwyer, Tian Tian, Xiaowei Zhang, Xiao Chen, Yingxing Li, Tom C. B. McLeish, Mark C. Leake*, Fan Bai*

*Corresponding author. Email: fbai@pku.edu.cn (F.B.); mark.leake@york.ac.uk (M.C.L.)

Published 20 October 2021, *Sci. Adv.* **7**, eabh2929 (2021)
DOI: 10.1126/sciadv.abh2929

The PDF file includes:

Supplementary Text
Figs. S1 to S8
Tables S1 to S5
Legends for movies S1 to S3
References

Other Supplementary Material for this manuscript includes the following:

Movies S1 to S3

Supplementary Text

Individual-based lattice model

Summary

We developed an individual-based lattice model that inferred parameters from the single-molecule experimental information from Slimfield microscopy to predict the collective behaviour (LLPS, FRAP) at the continuum level (*31*, *34*). The key ingredients to this model are 1) a discretization of the elongated cell geometry on a 1×3 μm^2 square lattice; 2) the diffusivities of- and interactions between proteins, and 3) the distinction between two classes of proteins, namely those that *drive* the formation of aggresomes by LLPS, and those that only weakly bind to the aggresomes and can serve as *probes* for aggresome formation (we interpreted the candidate aggresome biomarker proteins of EGFP labeled HslU, Kbl and AcnB as LLPS probes). In our modeling, we represented LLPS-driving proteins by a single mean-field-type protein 'A', and the probes by a protein `B'. As we show below, this distinction enabled us to describe LLPS by the number of A-proteins, N_A, its interaction energy, ε_{AA}, its diffusivity, D_A, but also the numerical choice of a lattice spacing, Δx, which affects the surface tension of the aggresome. For a diffusion length of Δx=4 nm, two aggresomes form in the experimentally relevant time scale of 1-2 hours with a diffusivity of D_A =0.2 $\mu m^2/s$. Regardless of the lattice spacing, the FRAP recovery curves require small diffusivities of the order $D_B=10^{-4}$ -10^{-3} $\mu m^2/s$ for the probes; our simulations are carried out at a computationally more feasible Δx=20 nm and D_A =6 $\cdot 10^{-3}$ $\mu m^2/s$ (details given below). As long as the number of B-proteins, N_B, remains sufficiently low, the FRAP curves can be described independently by a binding energy ε_{AB}, the diffusivities inside, $D_{B,in}$, and outside the aggresome, $D_{B,out}$, and the position and radius of the simulated laser that photobleaches the B-proteins. Below, we first detail the algorithm, then the choice of parameters to simulate LLPS, and finally the choice of parameters to simulate FRAP. Finally, we used our results to discuss the experimental variations in the FRAP curves measured for HslU, kbl and AcnB.

Algorithm

To model LLPS, the A-proteins were located at lattice sites and interacted through an attractive nearest-neighbour interaction energy ε_{AA}. In 2D, LLPS occurred when ε_{AA} was larger than the critical value of approximately 1.8 k_BT, with k_B the Boltzmann constant and T the absolute temperature (*33*) (the critical value of ε_{AA} depends on the type of lattice used, e.g., hexagonal, 2D, 3D, etc.: ε_{AA} should be considered a qualitative tuning parameter rather than an energy that is directly related to the structure of a real protein). Just above the critical value, the domain purity is low and the interfaces are wide and phase separation is difficult to distinguish, especially in the confined cell geometry. For increasing values of ε_{AA} the domain purity increased and the interfaces became sharper (the interface width is directly determined by Δx, and, like ε_{AA}, is dependent on the type of lattice used). Using a combined choice of the value of ε_{AA}, Δx and the number of proteins A, N_A, the experimental features of aggresome formation can be qualitatively reproduced. That is, in a range of Δx of 10-40 nm we found that a value $\varepsilon_{AA} = 2.2\ k_BT$ and an A-concentration of up to $100\% \times N_A / (1\times3\ \mu m^2 / \Delta x^2)$=40% A-rich droplets in an A-poor environment were formed. In our simulations, we included N_A=2,350 A proteins on a 50×150 lattice (the concentration is approximately 31.3%). For <2,000 A proteins, droplets mostly grew by ripening in contrast to the experiments where droplet fusion is observed.

In addition to protein A, our simulations also included 200 B protein molecules that probe the LLPS. This number was chosen to be sufficiently small to not affect the dynamics of A, but sufficiently large to collect enough statistics. This implies that within our model differences in copy number only affect the overall stoichiometry, but does not alter the physical trends; the number of B protein molecules in the simulation need not reflect the actual experimental copy number. In order to facilitate the diffusion of probe B into A-rich droplets, protein B may occupy the same site as protein A. In fact, diffusion of B into the aggresomes is promoted by an attractive interaction

energy ε_{AB}. The binding energy primarily affects the rate by which B may escape the aggresome and the partition of B inside, c_{in}, and outside, c_{out}, the aggresome. At thermal equilibrium the chemical potentials inside, μ_{in}, and outside, μ_{out}, the aggresomes are equal and given by $\mu_{in} = \Delta H + k_B T \ln c_{in} = \mu_{out} = \ln c_{out}$, with ΔH the binding enthalpy of protein B to the aggresome, so

$$\frac{c_{in}}{c_{out}} = exp(\Delta H / k_B T) \quad (1)$$

Collecting all interaction terms, the total internal energy is given by

$$U = N_{AA}\varepsilon_{AA} + N_{AB}\varepsilon_{AB} \quad (2)$$

with N_{AA} the number of nearest A-A neighbours and N_{AB} the number of lattice sites shared by A and B. This interaction energy biased the diffusion dynamics, which was modelled by enabling proteins to hop to the nearest-neighbour lattice sites. Using a simple kinetic Monte Carlo algorithm (*31*, *59*), at every time step, with a time increment discussed below, a random protein and hop direction was selected out of a list of N_{proc} potential processes (pseudo-random numbers are generated using the SIMD-oriented Fast Mersenne Twister (*60*)). If the hop was not forbidden (a site may not contain more than one A or B protein), the rate, r, of the process was calculated (see below). If the rate equals the maximum rate r_{max} (note that r_{max} corresponds to the bare hopping frequency, while interactions may only slow down the dynamics: $r \leq r_{max}$), the rate is accepted. If it is smaller, the rate is accepted but with a probability r/r_{max}. Regardless if a process is accepted or rejected, time is updated as

$$\Delta t = \frac{-\ln u}{N_{proc} r_{max}} \quad (3)$$

with u a uniform random number, $0<u\leq1$.
The rate of each process depends on which protein hops, as well as on the local environment of the protein. In general, the rate is given by

$$r = \nu \cdot min\left(1, exp(-\Delta U / k_B T)\right) \quad (4)$$

according to the Metropolis algorithm. The prefactor ν is, in absence of interactions, related to a diffusivity D as $\nu = D/\Delta x^2$. In our simulations with Δx=20 nm, we used D_A=6 10^{-3} μm^2/s to match the experimental time scale of the order of an hour to form two aggresomes (for Δx=4 nm the more realistic value of D_A=0.2 μm^2/s may be used; this would increase the simulation time by a factor >3000). The FRAP recovery curves are virtually unaffected by the lattice spacing with fixed diffusivities of B $D_{B,in}$=2 10^{-4} μm^2/s for when B hops between lattice sites that are co-occupied by A, $D_{B,out}$=10^{-3} μm^2/s when B hops between lattice sites that both do not contain A, and D=($D_{B,in}$ + $D_{B,out}$)/2 if one of the sites contain A.

Modelling of LLPS

We quantified the progress of LLPS using a characteristic length scale, R (t), obtained from the structure factor *(14)*. The structure factor, S (q), with q the wavenumber, was obtained by taking the Fourier transform of the configuration of the A proteins (visualised by the images in Fig. 3 and Fig. S6) and taking the angularly averaged square of the Fourier transform. The structure often had a low signal-to-noise ratio, and a numerically more robust value was obtained using the inverse Fourier transform, which is the correlation function, C(r) as a function of the distance r. In line with our previous work (*31*) we used the first minimum of C(r) to define the characteristic length scale. The measures S(q) and C(r) were displayed in Fig. S6A and S6B, respectively, for the simulation shown in Fig 3A in the main text.

To collect statistics, we ran every simulation for various random number seeds. While these may lead to qualitatively different late-stage (at the stage the droplet size approaches the size of the cell) structures, see Fig. S6C, for early times we expected the length scale to increase according to

the usual relation $R(t)–R_0 \sim t^{1/3}$ characteristic for Ostwald ripening and Brownian coalescence (*35*). Indeed, in Fig S4D we averaged this quantity (with R_0=0.03, 0.06 and 0.12 μm for Δx=10, 20, 40 nm, respectively) over 10 simulations and plotted it against time. We find that $R(t) - R_0 \propto (D_A\, t/\Delta\, x^2)^{1/3}$ up to a plateau where typically two aggresomes are formed. We have verified that the addition or removal of the B-proteins (up to 2.1 v%; well above the experimental concentration) did not significantly affect this growth curve; neither did the presence of an excluded volume region that may represent the nucleoid (Movie S3). The plateau is reached after approximately an hour when D_A=6 ·10^{-3} μm^2/s and Δx=20 nm. We extrapolate that the experimental value D_A=0.2 μm^2/s may be used when the lattice spacing is as small as Δx=4 nm. This value may slightly change when different values for ε_{AA} would be chosen. Furthermore, both the lattice spacing and ε_{AA} alter the width of the interface and may affect the respective contributions of Ostwald ripening and droplet fusion. Fortunately, the FRAP curves are unaffected by the lattice spacing. Therefore, we have chosen a computationally convenient lattice spacing of Δx=20 nm with a low A diffusivity of D_A =6 ·10^{-3} μm^2/s. For these values, the qualitative features of the aggresomes (Fig. S6C) and the time scale of aggresome formation (Fig. S6D) are in agreement with the experiments.

Modeling of FRAP

Motivated by our assumption that the dynamics of LLPS and fluorescent recovery could be decoupled, we set up idealized simulations where protein B can diffuse and interact with A-proteins whose spatial coordinates are kept constant to fix the aggresomes centres at 500 nm from the respective poles and their radius fixed at 400 nm (see Fig. S7A). While this size is somewhat larger than in the experiments and simulations with mobile A proteins, it does not affect the early stages of half-FRAP. We do expect that smaller aggresome sizes lead to a larger amplitude of whole-FRAP recovery. In Fig. S5B we showed reasonable consistency of the simulated FRAP curves between a simulation with Δx=10 nm and Δx=20 nm. In these simulations, we set the outside diffusivity to $D_{B,out}$=10^{-3} μm^2/s, as this gave the correct order of magnitude in the recovery time, and manually tuned the inside diffusivity, $D_{B,in}$, binding energy, ε_{AB}, and laser radius, R to match the experimental data. The fact that these values are much smaller than the mean values for the diffusivity measured (Fig 2B) suggests that the low-mobility tail of the distribution, possibly due to heterogeneity in the cytoplasm, determines the recovery on a macroscopic scale. We emphasize that a change in the choice of $D_{B,out}$ as well as the position of the laser in the half-FRAP simulations affects the final values. In these simulations we used a lattice spacing Δx=10 nm.

In Fig S7B we investigated the influence of the laser radius on the FRAP transients. While the half-FRAP curve was barely affected by variations of 380-400 nm, we found there was a narrow window just below 400 nm where the best match between whole-FRAP simulation and experiment were obtained. This radius, which was slightly smaller than the radius of the simulated aggresome, left some proteins at the rim of the aggresome unbleached and enabled them to govern fast, but low intensity, recovery. The need of a slightly smaller focus radius than the aggresome radius seems general in our simulations, and was also observed when LLPS and FRAP are simultaneously simulated. We speculate in the experiments the broad range of diffusivities also enables a small fraction of proteins to swiftly diffuse towards the aggresome and lead to fast initial recovery, and the sensitivity of FRAP signal on the laser focus may be weaker.

In Fig S5C we varied the binding energy, ε_{AB}, in the range 1.8-2.6 k_BT. In this range, the amplitude of the whole-FRAP curve monotonically decreased with an increasing binding energy due to an increasing concentration of B proteins inside the aggresome (see Eq. 1). At a value of approximately 2.5 k_BT the best agreement with the experimental whole-FRAP curve was found. - For the simulations where LLPS and FRAP were simultaneously modeled (i.e., with mobile A-proteins, see Fig. 3 in the main text) a value 2.2 k_BT gave a better match between the simulation and experiment. This suggests that the radius of the aggresomes and impurities (protein A present outside the aggresome, and vacant lattice sites inside the aggresome) affect the precise value of the

binding energy. Indeed using the experimental inside and outside concentrations (see Table S4), Eqn. 2 suggests a binding enthalpy of approximately 1.4 k_BT.

In Fig. S7D we varied the diffusivity of protein B inside the aggresome in the range $1\text{-}5\times10^{-4}$ $\mu m^2/s$ while keeping the outside diffusivity constant at 10^{-3} $\mu m^2/s$. In this case, the whole FRAP curve remains virtually unaffected, while the half FRAP recovery shift on the time axis proportional to the value of $D_{B,in}$. Using these simulations, we estimated the inside diffusivity to be approximately 2×10^{-4} $\mu m^2/s$. Like the value of the outside diffusivity, this rather small value suggests that heterogeneity/distribution in mobility in the cytoplasm limits the macroscopic recovery dynamics.

In summary, for a fixed bleaching position and radius, the simulated FRAP curves can be parameterized using the diffusivity of the probe protein inside and outside the aggresome, and the binding energy. In terms of these parameters we then interpreted the variations in the FRAP curves measured for the all three proteins HslU, Kbl and AcnB shown in Fig. S7E. Given that the half-FRAP curves are predominantly determined by the inside diffusivity, and consequently have a $\sim t^{1/2}$ time dependence, we shift the time axis such that the half-FRAP data collapses onto a master curve FRAP=$At^{1/2}$. We remark that the whole-FRAP recovery is achieved by a combination of diffusion inside the aggresome, exchange of proteins with the cytoplasm at short ranges and exchange of proteins between the two aggresomes at a long range: the apparent $t^{0.21}$ power law fitted to the whole-FRAP data is expected to be a purely heuristic effective fit to the model for all these processes combined. Figs. S5F-S5H show that after collapsing the half-FRAP data onto the master curve, the whole-FRAP data is now only affected by the outside diffusivity and by the binding energy. Indeed, if the outside diffusivity is low, then protein transport to the bleached area is small and the vertical offset of the whole FRAP curve decreases. If the binding energy is high, the protein concentration outside the aggresomes is low and the whole-FRAP signal also has a lower amplitude.

By applying this method to the experimental data we have obtained Fig S6H. Collapsing the half-FRAP data onto the master curve yielded estimates for the inside diffusivities of Kbl and AcnB to be 0.8 and 0.4 times the inside diffusivity of HslU, respectively. Further, the whole FRAP intensity decreased from Kbl to HslU to AcnB. The differences in the protein diffusivities may originate from differences in size and (energetic or hydrophobic) interactions with its environment. Within our model, we interpret that this decreased recovery rate originates from a lower concentration and/or a lower diffusivity of the respective proteins outside the aggresomes.

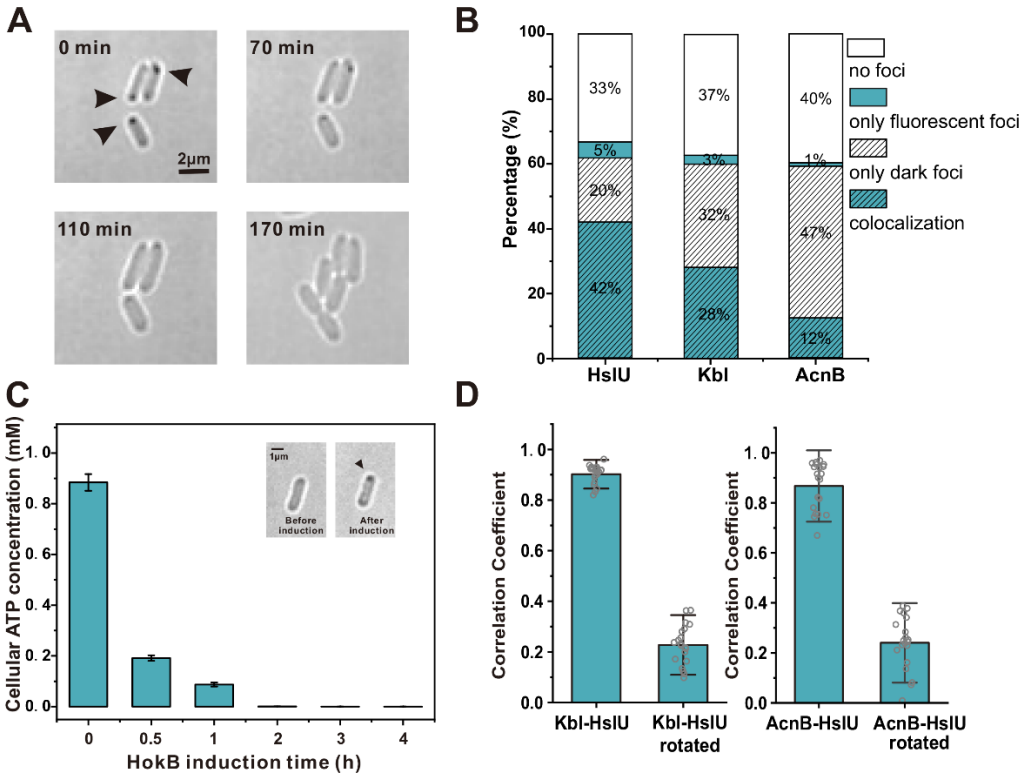

Fig. S1. Inducing HokB to stimulate aggresome formation.

(A) Brightfield images showing disassemble of ATP-dependent aggresome (black arrow) when cells experience fresh LB media. (B) Colocalization degree of brightfield dark foci and fluorescent foci of HslU-EGFP, Kbl-EGFP and AcnB-EGFP after 24 hrs culture. (C) Cellular ATP concentration as a HokB induction time. (Insert: brightfield images of the cell before and after HokB induction, error bar indicates SD.) (D) Colocalization analysis of HslU-mCherry & Kbl-EGFP fluorescent foci and HslU-mCherry & AcnB-EGFP fluorescent foci after 5 hrs HokB induction (only cells with fluorescent foci in both mCherry and EGFP channels were analyzed, N=20 for each group, error bar indicates SD). (left) Pearson's correlation coefficients of HslU-mCherry fluorescent foci and Kbl-EGFP fluorescent foci of cells overexpressing HokB before and after rotating HslU-mCherry image by 90 degrees. (right) Pearson's correlation coefficients of HslU-mCherry fluorescent foci and AcnB-EGFP fluorescent foci of cells overexpressing HokB before and after rotating HslU-mCherry image by 90 degrees.

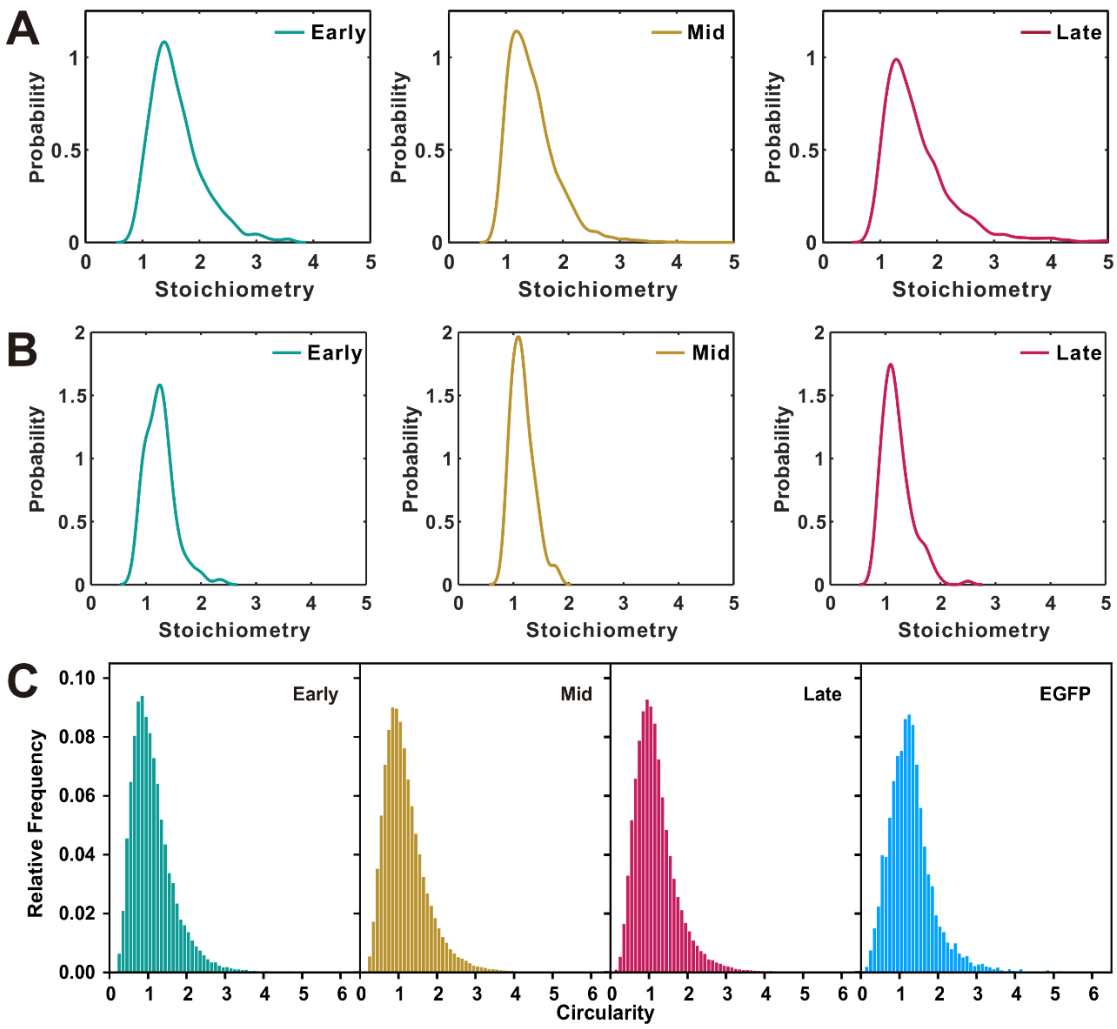

Fig. S2. HslU stoichiometry and circularity

(A) Kernel density plots of stoichiometry of HslU-EGFP per focus from tracks found from 500 frames until the end of imaging at different HokB induction stages. (B) Kernel density plots of stoichiometry of HslU-EGFP per focus from tracks found at the end of photobleach process (from 1500 frames of the start of laser illumination until the end) at different HokB induction stages. All the peaks are around 1, which confirmed that the tracks for defining *Dg* are single molecules. (C) Circularity of single-molecule spots and surface-immobilized EGFP.

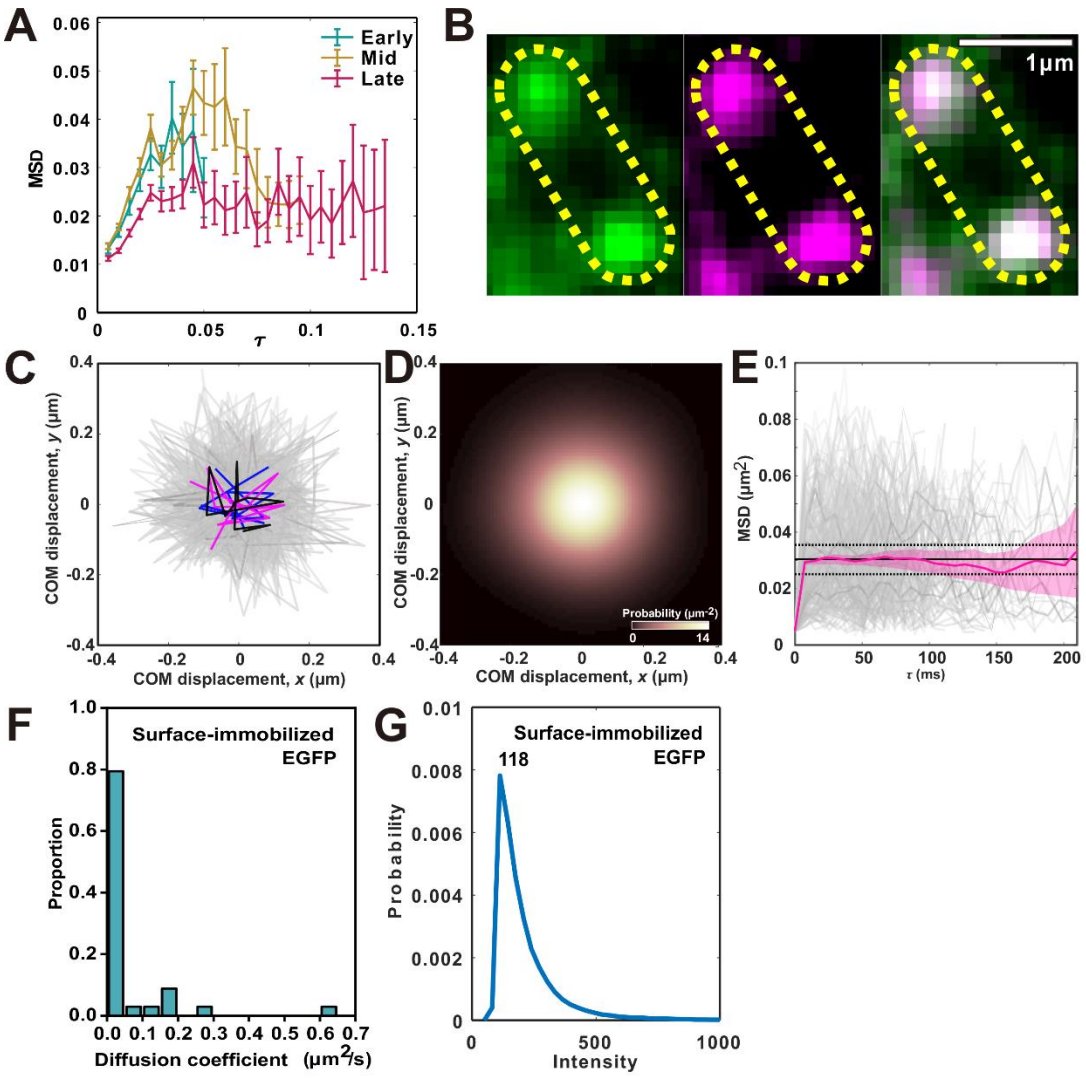

Fig. S3. HslU mobility

(A) Time versus MSD relations at the different HokB induction stages. The maximum observed mean average MSD values in the plots were used for defining diameters of aggresomes at the different HokB induction stages. (B) PALM imaging of live HslU-mMaple3 cells at late stage: average intensity projections under widefield 488 nm (green, left) and photoswitching 405 nm + 561nm wavelength excitation (magenta, center); merge (right). (C) Displacements (relative to track center of mass, COM) overlaid for all tracked mMaple3 (n=583 tracks from N=23 aggresomes); three randomly selected tracks are highlighted. (D) Displacements (relative to COM) displayed as a probability density heatmap (kernel density width of 70 nm approximate localization precision in each PALM frame) indicating an upper bound for the confinement. (E) The mean-square pairwise displacements as a function of time interval along the tracks, τ, are shown for the individual tracks (gray); the mean MSD at each time interval (magenta line) and its 95% confidence interval (shaded area) are overlaid. The mean MSD plateau value (solid black line) ± SD (dashed lines) is weighted for the number of tracks at each time interval greater than two frames. (F) Histogram of the diffusion coefficients of surface-immobilized EGFP (number of molecules N=34). (G) The value of single intensity (118 counts) is the characteristic intensity of surface-immobilized EGFP molecule obtained using an *in vitro* assay for purified EGFP under the same imaging conditions (*29*).

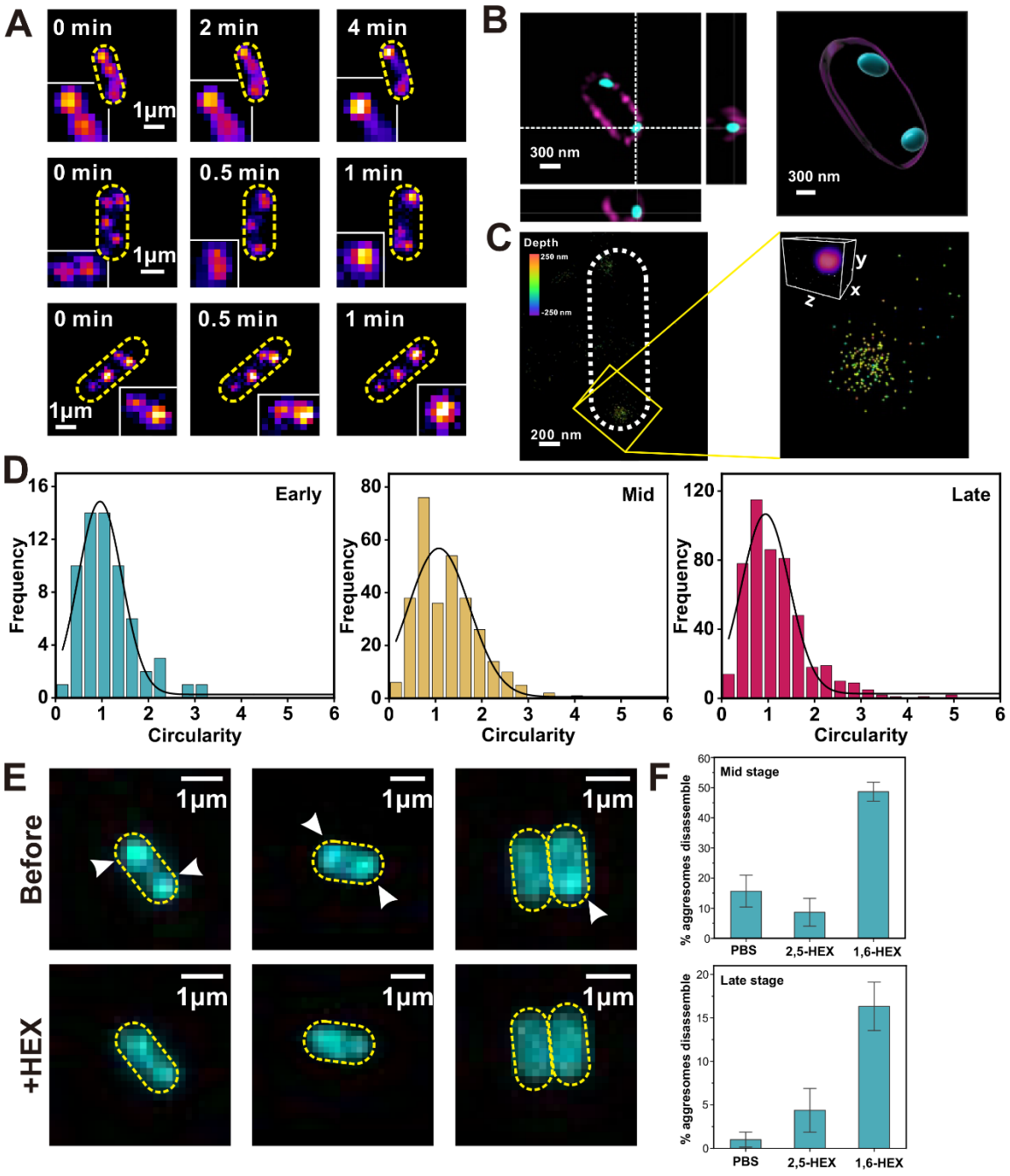

Fig. S4. Aggresome fusion.

(A) Fluorescence images of two aggresomes fusing. (B) 3D-SIM images of a typical cell at late stage of aggresome formation (cyan: HslU-EGFP, magenta: cell membrane stained by FM4-64). Left: orthogonal view images. Right: 3D view rendering images. (C) Left: 3D-STORM images of a representative cell at late stage. Different color represents different depth. Right: a zoom-in image of an aggresome. The number of molecules of the zoom-in area is 164. Inset: 3D-reconstruction of the aggresome. (D) Circularity of the aggresome at the different stages. Early: 0.96 ± 0.06, Mid: 1.07 ± 0.01, Late: 1.03 ± 0.01. (E) Fluorescence images of cells before and after HEX treatment. (F) Disassembly ratio of aggresomes under 1,6-HEX treatment. PBS and 2,5-HEX were chosen as negative controls.

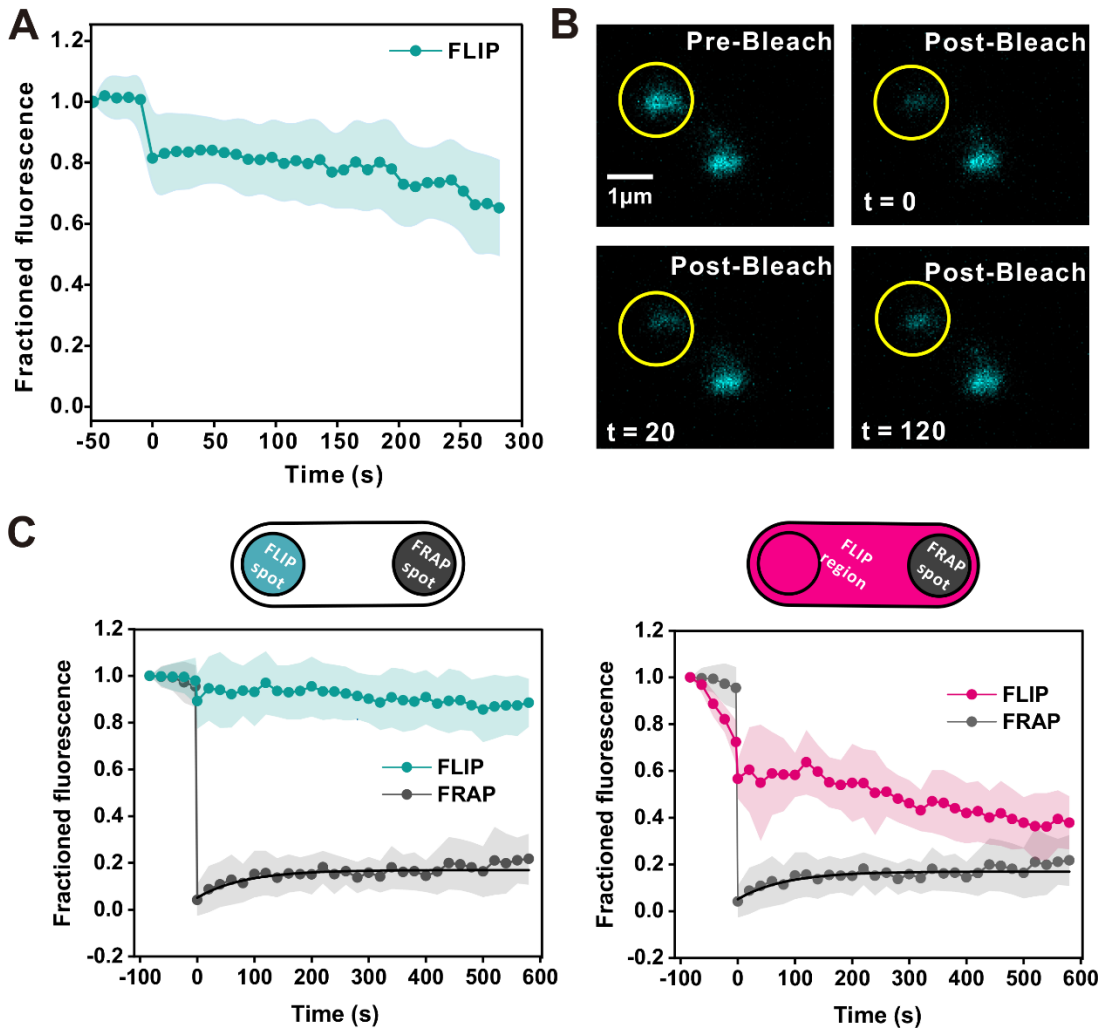

Fig. S5. HslU turnover.

(A) Mean half-FLIP trace (number of aggresomes N=29). The focused laser has a diameter of approximately 0.65 µm, so on average the cytoplasmic pool of bleached HslU-EGFP for a typical 3 µm long cell is ~1/4 whereas the cytoplasmic pool of unbleached HslU-EGFP is ~3/4 of the total cell area. If there is turnover between cytoplasm and aggresome (as we observe from whole-FRAP experiments) then a larger unbleached EGFP pool increases the apparent net rate of recovery of intensity in half-FRAP compared to the apparent rate of loss of intensity in half-FLIP. (B) Fluorescence images of an example whole-FRAP experiment showing fluorescence recovery from the bleached aggresome over time, half-time recovery constant 32 ± 18 s. (C) Left: Mean fluorescence recovery curve from the bleached aggresome and mean fluorescence loss from a second aggresome in the cell for cells that only contained two detectable aggresomes. Right: Mean fluorescence recovery curve from the bleached aggresome and mean fluorescence loss from all the entire cell area apart for the bleached aggresome.

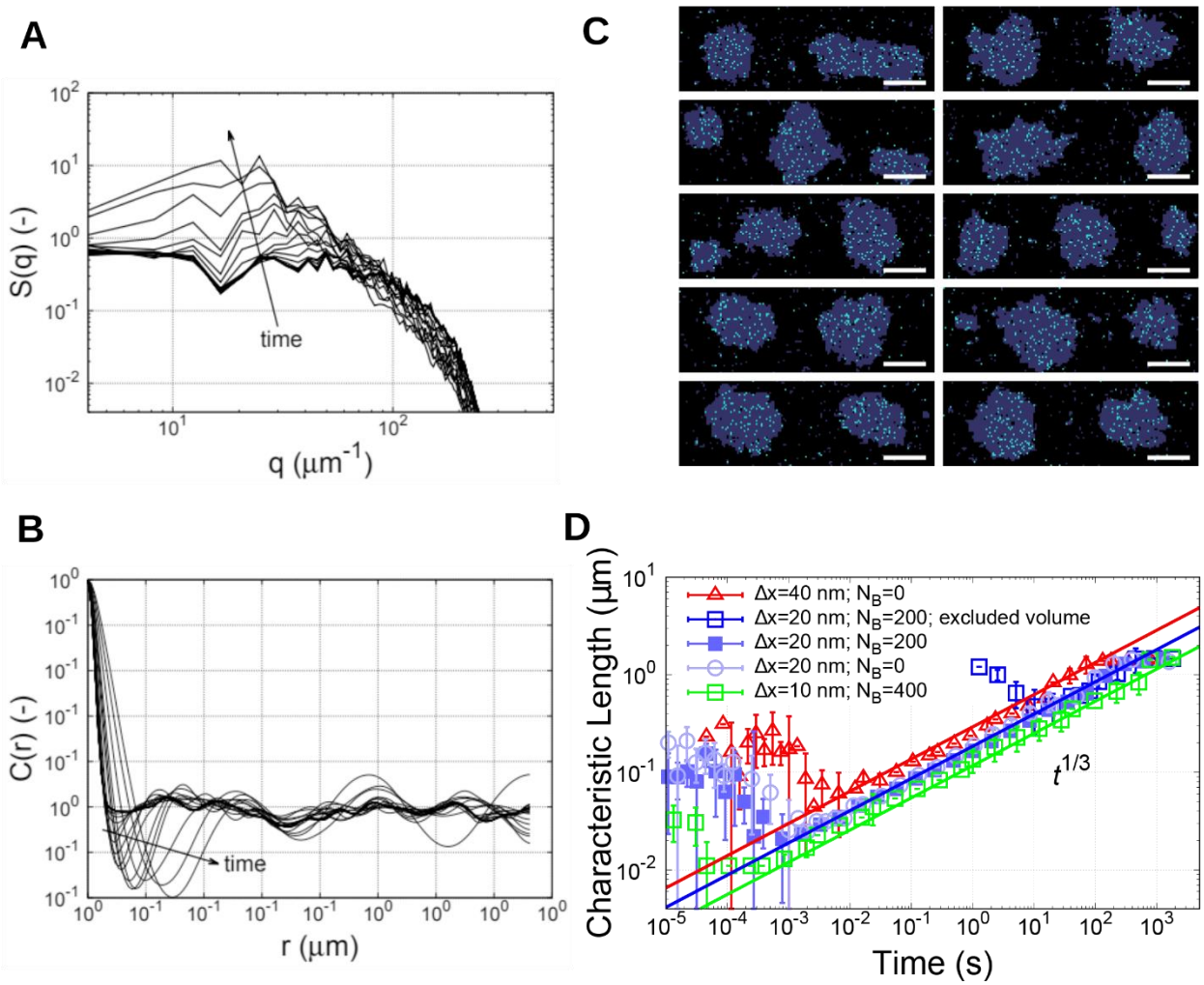

Fig. S6. Quantification of LLPS

(A) The structure factor, *S(q)*, against the wavenumber, q, as calculated from the configuration of protein A in the morphology images in Fig. 3 in the main text. As time proceeds, a peak emerges that shifts to decreasing wavenumbers. (B) The correlation function, *C(r)* against length scale, r, as determined from the structure factor in panel A. The first minimum is used as the characteristic length scale of the morphology. (C) Variations in morphology after 10^9 time steps (approximately 8,500 seconds of simulated real time) for 10 different random number seeds. Typically, after this time two or three droplets have formed. The scale bar represents 500 nm. (D) The characteristic length scale is plotted against time for simulations with and without proteins B present and for two lattice spacings. The influence of protein B on LLPS is negligible. The lattice spacing does affect the rate of LLPS due to its influence on the surface tension.

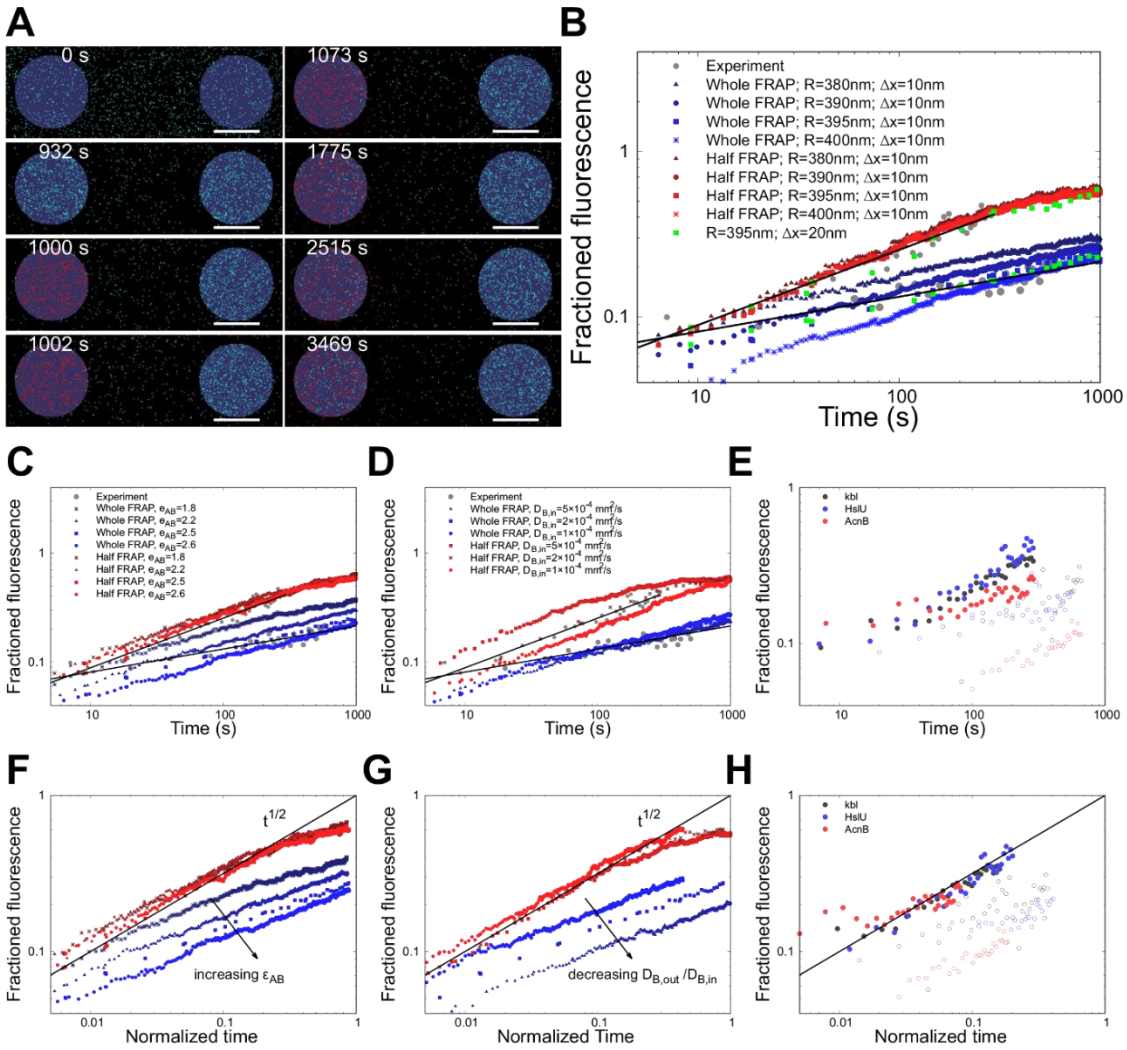

Fig. S7 Exploring parameter space in simulations.
The influence of the inside, $D_{B,in}$, and outside diffusivity, $D_{B,out}$, and the binding energy, ε_{AB}, on FRAP transients is investigated. (A) The diffusion of protein B is simulated while protein A is fixed in perfectly round aggresomes with a 400 nm radius. At t=0 B is randomly distributed; after being equilibrated for 1000 seconds protein B is bleached within a simulated focus. The scale bar represents 500 nm. (B) Variations of the radius of the laser focus predominantly affected whole FRAP transients, while the half-FRAP transients were insensitive to this variation. (C-D) For a fixed laser position, the binding energy (C) and inside diffusivity (D) are varied, which predominantly affected the whole and the half FRAP data, respectively. (E) The experimental differences in FRAP transients between the three proteins klb, HslU and AcnB; the closed and open circles represent half- and whole-FRAP measurement, respectively. (F-H) To interpret the experimental data of (E), the time scale of (C-D) is normalized by collapsing the half FRAP data onto the master curve FRAP=$A\ t^{1/2}$. The prefactor A provides values for the diffusivities of the proteins inside the aggresome. The remaining variations in the whole FRAP data are interpreted to originate from a combination of differences in the outside diffusivity and binding energy.

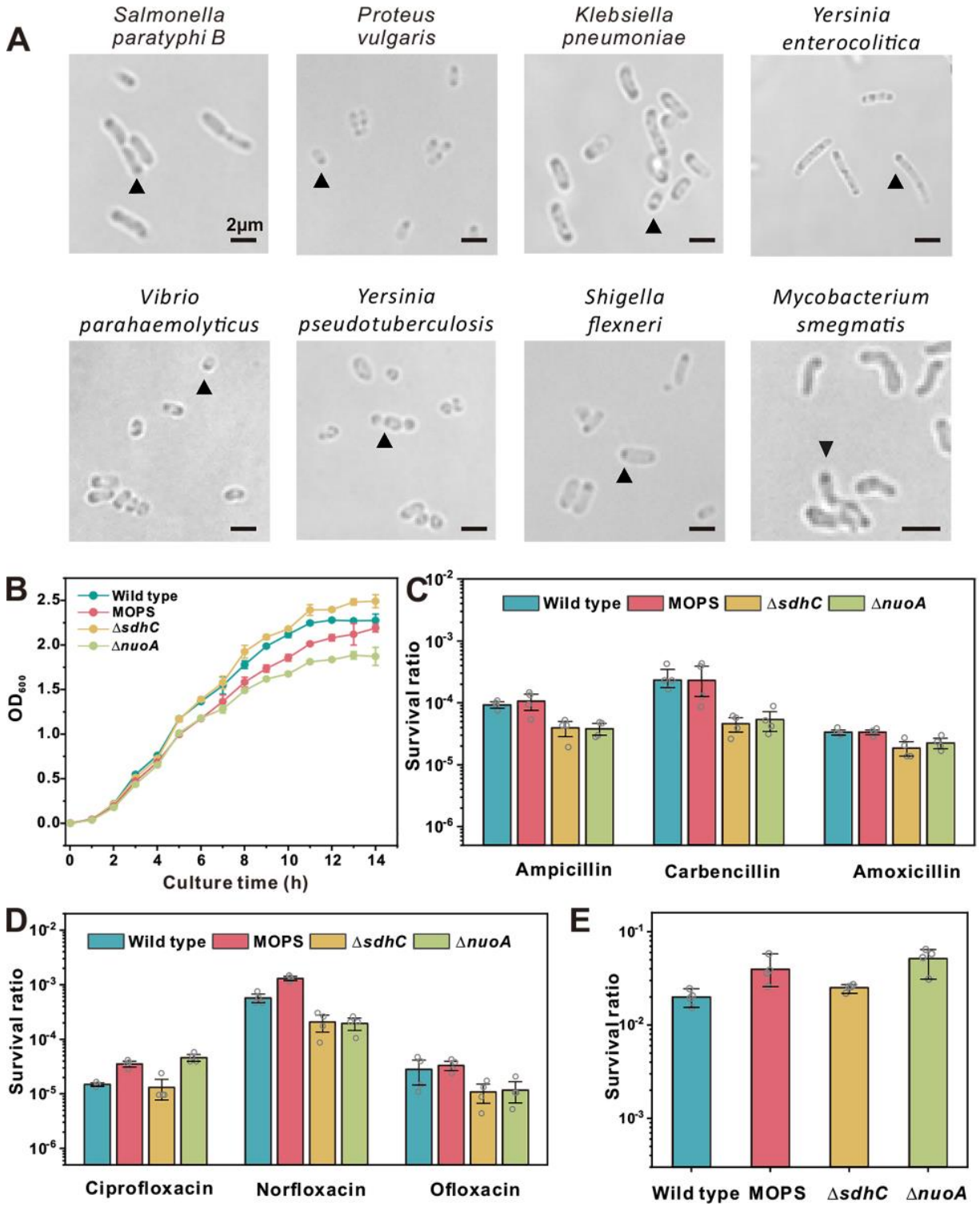

Fig S8. Role of LLPS in bacterial fitness.

(A) Brightfield images of different Gram-negative bacterial species in late stationary phase. Aggresome formation (black arrow) is widely observed. (B) Growth curve of different strains (wild type, MOPS, Δ*sdhC* and Δ*nuoA*). (C) Cell survival rate after 4 hrs β-lactam antibiotic treatment of different strains cultured in LB for 12 hrs. (D) Cell survival rate after 4 hrs fluoroquinolone antibiotic treatment of different strains cultured in LB for 12 hrs. (E) Cell survival rate after P1 phage infection (MOI=100) of different strains cultured in LB for 12 hrs (error bar indicates SE).

Table S1. Strains used in this study.

Bacterial Strains	Source	Genotype	Doubling time (min)
MG1655	Yale Genetic Stock Center(CGSC#:6300)	Wild-type	23.5 ±0.7
HslU-EGFP	LAB strain	MG1655 *ΔaraD-B* hslU::EGFP	23.4 ±0.8
HslU-mMaple3	LAB strain	MG1655 *ΔaraD-B* hslU::mMaple3	25.2±1.1
Kbl-EGFP	LAB strain	MG1655 *ΔaraD-B* kbl::EGFP	24.0 ±1.6
AcnB-EGFP	LAB strain	MG1655 *ΔaraD-B* acnB::EGFP	23.6 ±0.8
Kbl-EGFP & HslU-mCherry	LAB strain	MG1655 *ΔaraD-B* kbl::EGFP hslU::mCherry	25.9 ±1.3
AcnB-EGFP & HslU-mCherry	LAB strain	MG1655 *ΔaraD-B* acnB::EGFP hslU::mCherry	25.7 ±1.2
ΔnuoA	LAB strain	MG1655 *ΔnuoA*	22.7 ±1.5
ΔsdhC	LAB strain	MG1655 *ΔsdhC*	23.4 ±0.5
ΔnuoA & HslU-EGFP	LAB strain	MG1655 *ΔaraD-B ΔnuoA* hslU::EGFP	23.5 ±1.2
ΔsdhC & HslU-EGFP	LAB strain	MG1655 *ΔaraD-B ΔsdhC* hslU::EGFP	24.1 ±0.8

Table S2. Plasmids used in this study.

Name	Gene	Resistance
pBAD-hokB	araBAD-hokB	Chloramphenicol
pSIM6	(*50*)	Ampicillin
pCP20	(*61*)	Ampicillin

Table S3. Primers used in this study.

Name	Sequence (5'-3')
araB-D knockout F	GTTTCTCCATACCCGTTTTTTTGGATGGAGTGAAACGATGATTCCGGGGATCCGTCGACC
araB-D knockout R	GCTGTGGTTTTATACAGTCATTACTGCCCGTAATATGCCTTTGTAGGCTGGAGCTGCTTCG
hslU+EGFP homology F	TGCGTTGGTGGCAGATGAAGATCTGAGCCGTTTTATCCTAGGTGGATCCGGCGGTTCTGTGAG
hslU+EGFP homology R	TTCAGCCCCATCAAACAATGATGAAAATGATTGAACGCGAGCTACCGCCACTGCCACCGCTC
hslU+EGFP P1	GGCGACGGCCCCGTGCTGCT
hslU+EGFP P2	GAACGCGATTACTTGTACAGCTCGTCCA
hslU+EGFP P3	ACAAGTAATCGCGTTCAATCATTTTCAT
hslU+EGFP P4	CAGCAAAGGCGAGGGGGAGG
acnB+EGFP homology F	CACCGAGAAAGCCGATGGGGTGATTTTCCAGACTGCGGTTGGTGGATCCGGCGGTTCTGTGAG
acnB +EGFP homology R	GGGCATTGTGTCGTTTATGCGCAGCGCGTGCGCTGACTTTGCTACCGCCACTGCCACCGCTC
acnB+EGFP P1	GGCGACGGCCCCGTGCTGCT
acnB+EGFP P2	CTGACTTTTTACTTGTACAGCTCGTCCA
acnB+EGFP P3	ACAAGTAAAAAGTCAGCGCACGCGCTGC
acnB+EGFP P4	CCGGCAATGCACCGAAAT
kbl+EGFP homology F	AGCATTTACGCGTATTGGTAAACAACTGGGCGTTATCGCCGGTGGATCCGGCGGTTCTGTGAG
kbl +EGFP homology R	CTTCCGCTTTCAGTTTGGATAACGCTTTCATCTCACATCCGCTACCGCCACTGCCACCGCTC
kbl+EGFP P1	GGCGACGGCCCCGTGCTGCT
kbl+EGFP P2	TCACATCCTTACTTGTACAGCTCGTCCA
kbl+EGFP P3	ACAAGTAAGGATGTGAGATGAAAGCGTT
kbl+EGFP P4	CGACCACTCATCCCAGTT
Cat(HslU)-F	CACCATCGAAGAATTAAGCTACAAAGCGTAAGGATCTCCCTCTAGAGCGACGCCAGACGG
Cat(HslU)-R	TTCAGCCCCATCAAACAATGATGAAAATGATTGAACGCGATTACGCCCCGCCCTGCCACT

HslU-F	ATGTCTGAAATGACCCCACGC
HslU-R	GAGCCACCTAGGATAAAACGGCTCAGATCTTCATCTGC
Linker-mCherry-F	TTATCCTAGGTGGCTCTGGTGGCGGTTC
mCherry-R	TTACTTGTACAGCTCGTCCATGCCG
Homo-HslU-F	CACCATCGAAGAATTAAGCTACAAAGCGTAAGGATCTCCCATGTCTGAAATGACCCCACG
Homo-mCherry-R	TTCAGCCCCATCAAACAATGATGAAAATGATTGAACGCGATTACTTGTACAGCTCGTCCATGCCG
sdhC knockout F	CCCAGGGAATAATAAGAACAGCATGTGGGCGTTATTCATGTCTAGAGCGACGCCAGACGG
sdhC knockout R	CCTAATGCGGAGGCGTTGCTTACCATACGAGGACTCCTGCTGTAGGCTGGAGCTGCTTCG
nuoA knockout F	GAGCAGTGAATCTGGCGCTACTTTTGATGAGTAAGCAATGATTCCGGGGATCCGTCGACC
nuoA knockout R	CCATCTTAATGCCTCGCGGTTAGCGTTGACGATTAGCGATTGTAGGCTGGAGCTGCTTCG

Table S4. Information of aggresomes.

Number of HslU-EGFP molecules per cell at different incubation stages, with estimates of aggresome volume based on measurements of aggresome diameter from MSD analysis and assuming a spherical shape. Errors indicated are standard deviation, number of cells measured in range 31-209. Aggregation enthalpy (ΔH) of HslU in the early, mid and late stages. The aggregation enthalpies are calculated using Eq. (1), where the outside concentration is estimated as $c_{out}=(N_{cell}-N_{agg})/(V_{cell}-V_{agg})$.

	Early	Mid	Late
Number of aggresome per cell	2.0	2.4	2.3
Number of protein per cell	276 ± 253	510 ± 345	681 ± 437
Number of protein per aggresome	35 ± 20	50 ± 32	63 ± 35
Mean cytoplasmic viscosity (cP)	6.2	8.3	16.6
c_{in}/c_{out}	4.27 ± 0.42	5.11 ± 1.26	3.78 ± 0.11
$\Delta H/k_BT$	1.45 ± 0.10	1.53 ± 0.25	1.33 ± 0.03
Volume of aggresome (μm^3)	0.050 ± 0.008	0.055 ± 0.008	0.046 ± 0.009

*

Table S5. Molecular mobility of HslU-EGFP, Kbl-EGFP and AcnB-EGFP inside aggresomes.

	D_g-D_a ($\mu m^2/s$), ± SE	Number of cells	Number of aggresomes
HslU	0.10 ± 0.03	370	858
Kbl	0.14 ±0.08	435	798
AcnB	0.23 ± 0.01	737	1194

Movie S1

Half-FRAP imaging. By focusing a laser laterally offset approximately 0.5 μm from the center of an aggresome it was possible to photobleach approximately one half while leaving the other half intact, which we denote as "half-FRAP". We then measured the aggresome fluorescence intensity at 10 secs intervals for up to several hundred seconds after the focused laser bleach. (White dot: Bleached half-aggresome.)

Movie S2

Half-FRAP simulation. The size of the cell is 1×3 μm and the volume fraction of LLPS-driving protein A is 31% (gray) and LLPS-probing protein B (unbleached: cyan; bleached: red) is 2.7% In the simulations, the aggresomes emerge and coarsen for 158 minutes, after which protein B is bleached (colored red) within a simulated laser focus region.

Movie S3

Simulation with excluded volume. Aggresome formation simulation with a circular excluded volume region with a radius of 400 nm in the center of the cell. The size of the cell is 1×3 μm and the volume fraction of LLPS-driving protein A is 31% (gray) and LLPS-probing protein B (cyan) is 2.7%. The time scales of coarsening are similar to simulations without an excluded volume region.

REFERENCES AND NOTES

1. S. Alberti, A. Gladfelter, T. Mittag, Considerations and challenges in studying liquid-liquid phase separation and biomolecular condensates. *Cell* **176**, 419–434 (2019).
2. A. A. Hyman, C. A. Weber, F. Juelicher, Liquid-liquid phase separation in biology. *Annu. Rev. Cell Dev. Biol.* **30**, 39–58 (2014).
3. F. Wippich, B. Bodenmiller, M. G. Trajkovska, S. Wanka, R. Aebersold, L. Pelkmans, Dual specificity kinase DYRK3 couples stress granule condensation/dissolution to mTORC1 signaling. *Cell* **152**, 791–805 (2013).
4. C. P. Brangwynne, T. J. Mitchison, A. A. Hyman, Active liquid-like behavior of nucleoli determines their size and shape in *Xenopus laevis* oocytes. *Proc. Natl. Acad. Sci. U.S.A.* **108**, 4334–4339 (2011).
5. C. P. Brangwynne, C. R. Eckmann, D. S. Courson, A. Rybarska, C. Hoege, J. Gharakhani, F. Juelicher, A. A. Hyman, Germline P granules are liquid droplets that localize by controlled dissolution/condensation. *Science* **324**, 1729–1732 (2009).
6. J. van den Berg, A. J. Boersma, B. Poolman, Microorganisms maintain crowding homeostasis. *Nat. Rev. Microbiol.* **15**, 309–318 (2017).
7. L. Shapiro, H. H. McAdams, R. Losick, Why and how bacteria localize proteins. *Science* **326**, 1225–1228 (2009).
8. M. R. Alley, J. R. Maddock, L. Shapiro, Polar localization of a bacterial chemoreceptor. *Genes Dev.* **6**, 825–836 (1992).
9. Z. Hu, J. Lutkenhaus, Topological regulation of cell division in *Escherichia coli* involves rapid pole to pole oscillation of the division inhibitor MinC under the control of MinD and MinE. *Mol. Microbiol.* **34**, 82–90 (1999).
10. N. Al-Husini, D. T. Tomares, O. Bitar, W. S. Childers, J. M. Schrader, α-Proteobacterial RNA degradosomes assemble liquid-liquid phase-separated RNP bodies. *Mol. Cell* **7**1, 1027–1039.14 (2018).
11. B. Guilhas, J.-C. Walter, J. Rech, G. David, N. O. Walliser, J. Palmeri, C. Mathieu-Demaziere, A. Parmeggiani, J.-Y. Bouet, A. Le Gall, M. Nollmann, ATP-driven separation of liquid phase condensates in bacteria. *Mol. Cell* **79**, 293–303.e4 (2020).
12. A.-M. Ladouceur, B. S. Parmar, S. Biedzinski, J. Wall, S. G. Tope, D. Cohn, A. Kim, N. Soubry, R. Reyes-Lamothe, S. C. Weber, Clusters of bacterial RNA polymerase are biomolecular condensates

that assemble through liquid-liquid phase separation. *Proc. Natl. Acad. Sci. U.S.A.* **117**, 18540–18549 (2020).

13. N. G. Bednarska, J. Schymkowitz, F. Rousseau, J. Van Eldere, Protein aggregation in bacteria: The thin boundary between functionality and toxicity. *Microbiology* **159**, 1795–1806 (2013).
14. C. Bollen, L. Dewachter, J. Michiels, Protein aggregation as a bacterial strategy to survive antibiotic treatment. *Front. Mol. Biosci.* **8**, e669664 (2021).
15. J. Winkler, A. Seybert, L. König, S. Pruggnaller, U. Haselmann, V. Sourjik, M. Weiss, A. S. Frangakis, A. Mogk, B. Bukau, Quantitative and spatio-temporal features of protein aggregation in *Escherichia coli* and consequences on protein quality control and cellular ageing. *EMBO J.* **29**, 910–923 (2010).
16. S. Kaushik, A. M. Cuervo, Proteostasis and aging. *Nat. Med.* **21**, 1406–1415 (2015).
17. C. M. Dobson, Principles of protein folding, misfolding and aggregation. *Semin. Cell Dev. Biol.* **15**, 3–16 (2004).
18. A. B. Lindner, R. Madden, A. Demarez, E. J. Stewart, F. Taddei, Asymmetric segregation of protein aggregates is associated with cellular aging and rejuvenation. *Proc. Natl. Acad. Sci. U.S.A.* **105**, 3076–3081 (2008).
19. S. K. Govers, J. Mortier, A. Adam, A. Aertsen, Protein aggregates encode epigenetic memory of stressful encounters in individual *Escherichia coli* cells. *PLOS Biol.* **16**, e2003853 (2018).
20. J. Mortier, W. Tadesse, S. K. Govers, A. Aertsen, Stress-induced protein aggregates shape population heterogeneity in bacteria. *Curr. Genet.* **65**, 865–869 (2019).
21. Y. Pu, Y. Li, X. Jin, T. Tian, Q. Ma, Z. Zhao, S. Lin, Z. Chen, B. Li, G. Yao, M. C. Leake, C.-J. Lo, F. Bai, ATP-dependent dynamic protein aggregation regulates bacterial dormancy depth critical for antibiotic tolerance. *Mol. Cell* **73**, 143–156.e4 (2019).
22. M. Leslie, Sloppy science or groundbreaking idea? Theory for how cells organize contents divides biologists (Science AAAS, 2021); www.sciencemag.org/news/2021/01/sloppy-science-or-groundbreaking-idea-theory-how-cells-organize-contents-divides.
23. C. A. Azaldegui, A. G. Vecchiarelli, J. S. Biteen, The emergence of phase separation as an organizing principle in bacteria. *Biophys. J.* **120**, 1123–1138 (2021).
24. D. Wilmaerts, M. Bayoumi, L. Dewachter, W. Knapen, J. T. Mika, J. Hofkens, P. Dedecker, G. Maglia, N. Verstraeten, J. Michiels, The persistence-inducing toxin hokB forms dynamic pores that cause ATP leakage. *MBio* **9**, e00744-18 (2018).

25. R. Reyes-Lamothe, D. J. Sherratt, M. C. Leake, Stoichiometry and architecture of active dna replication machinery in *Escherichia coli*. *Science* **328**, 498–501 (2010).
26. S. M. D. Oliveira, R. Neeli-Venkata, N. S. M. Goncalves, J. A. Santinha, L. Martins, H. Tran, J. Makela, A. Gupta, M. Barandas, A. Hakkinen, J. Lloyd-Price, J. M. Fonseca, A. S. Ribeiro, Increased cytoplasm viscosity hampers aggregate polar segregation in *Escherichia coli. Mol. Microbiol*. **99**, 686–699 (2016).
27. C. W. Mullineaux, A. Nenninger, N. Ray, C. Robinson, Diffusion of green fluorescent protein in three cell environments in *Escherichia col*i. *J. Bacteriol.* **188**, 3442–3448 (2006).
28. M. C. Leake, J. H. Chandler, G. H. Wadhams, F. Bai, R. M. Berry, J. P. Armitage, Stoichiometry and turnover in single, functioning membrane protein complexes. *Nature* **443**, 355–358 (2006).
29. S. Kroschwald, S. Maharana, A. Simon, Hexanediol: A chemical probe to investigate the material properties of membrane-less compartments. *Matters* **3**, e201702000010 (2017).
30. C. Schaefer, S. Paquay, T. C. B. Mcleish, Morphology formation in binary mixtures upon gradual destabilisation. *Soft Matter* **15**, 8450–8458 (2019).
31. A.-S. Coquel, J.-P. Jacob, M. Primet, A. Demarez, M. Dimiccoli, T. Julou, L. Moisan, A. B. Lindner, H. Berry, Localization of protein aggregation in *Escherichia coli* is governed by diffusion and nucleoid macromolecular crowding effect. *PLoS Comput. Biol*. **9**, e1003038 (2013).
32. K. Huang, *Statistical Mechanics* (John Wiley & Sons, 2nd ed., 1987).
33. D. W. Heermann, K. Binder, *Monte Carlo Simulation in Statistical Physics: An Introduction. Graduate Texts in Physics* (Springer International Publishing, 2019).
34. J. D. Gunton, M. S. Miguel, P. S. Sahni, *Phase Transitions and Critical Phenomena* (Academic Press, 2001).
35. A. Narayanan, A. Meriin, J. O. Andrews, J.-H. Spille, M. Y. Sherman, I. I. Cisse, A first order phase transition mechanism underlies protein aggregation in mammalian cells. *eLife* **8**, e39695 (2019).
36. D. Leszczynska, E. Matuszewska, D. Kuczynska-Wisnik, B. Furmanek-Blaszk, E. Laskowska, The formation of persister cells in stationary-phase cultures of *Escherichia coli* is associated with the aggregation of endogenous proteins. *PLOS ONE* **8**, e54737 (2013).
37. J. Yu, Y. Liu, H. Yin, Z. Chang, Regrowth-delay body as a bacterial subcellular structure marking multidrug-tolerant persisters. *Cell Discov*. **5**, 8 (2019).
38. S. Cayley, M. Record Jr, B. Lewis, Accumulation of 3-(n-morpholino)propanesulfonate by osmotically stressed *Escherichia coli* K-12. *J. Bacteriol.* **171**, 3597–3602 (1989).

39. B. R. Parry, I. V. Surovtsev, M. T. Cabeen, C. S. O'Hem, E. R. Dufresne, C. Jacobs-Wagner, The bacterial cytoplasm has glass-like properties and is fluidized by metabolic activity. *Cell* **156**, 183–194 (2014).
40. S. Kroschwald, M. C. Munder, S. Maharana, T. M. Franzmann, D. Richter, M. Ruer, A. A. Hyman, S. Alberti, Different material states of Pub1 condensates define distinct modes of stress adaptation and recovery. *Cell Rep*. **23**, 3327–3339 (2018).
41. E. W. J. Wallace, J. L. Kear-Scott, E. V. Pilipenko, M. H. Schwartz, P. R. Laskowski, A. E. Rojek, C. D. Katanski, J. A. Riback, M. F. Dion, A. M. Franks, E. M. Airoldi, T. Pan, B. A. Budnik, D. A. Drummond, Reversible, specific, active aggregates of endogenous proteins assemble upon heat stress. *Cell* **162**, 1286–1298 (2015).
42. R. Giraldo, C. Fernández, M. Moreno-del Álamo, L. Molina-García, A. Revilla-García, M. Cruz Sanchez-Martínez, J. F. Gimenez-Abián, S. Moreno-Díaz de la Espina, RepA-WH1 prionoid: Clues from bacteria on factors governing phase transitions in amyloidogenesis. *Prion* **10**, 41–49 (2016).
43. J. Kwiatkowska, E. Matuszewska, D. Kuczynska-Wisnik, E. Laskowska, Aggregation of *Escherichia coli* proteins during stationary phase depends on glucose and oxygen availability. *Res. Microbiol*. **159**, 651–657 (2008).
44. J.-U. Dahl, M. J. Gray, U. Jakob, Protein quality control under oxidative stress conditions. *J. Mol. Biol*. **427**, 1549–1563 (2015).
45. J. Ling, C. Cho, L.-T. Guo, H. R. Aerni, J. Rinehart, D. Söll, Protein aggregation caused by aminoglycoside action is prevented by a hydrogen peroxide scavenger. *Mol. Cell* **48**, 713–722 (2012).
46. A. Patel, L. Malinovska, S. Saha, J. Wang, S. Alberti, Y. Krishnan, A. A. Hyman, ATP as a biological hydrotrope. *Science* **356**, 753–756 (2017).
47. K. A. Datsenko, B. L. Wanner, One-step inactivation of chromosomal genes in *Escherichia coli* K-12 using PCR products. *Proc. Natl. Acad. Sci. U.S.A.* **97**, 6640–6645 (2000).
48. S. Datta, N. Costantino, D. L. Court, A set of recombineering plasmids for gram-negative bacteria. *Gene* **379**, 109–115 (2006).
49. M. J. Giacalone, A. M. Gentile, B. T. Lovitt, N. L. Berkley, C. W. Gunderson, M. W. Surber, Toxic protein expression in *Escherichia coli* using a rhamnose-based tightly regulated and tunable promoter system. *Biotechniques* **40**, 355–364 (2006).

50. T. Baba, T. Ara, M. Hasegawa, Y. Takai, Y. Okumura, M. Baba, K. A. Datsenko, M. Tomita, B. L. Wanner, H. Mori, Construction of *Escherichia coli* K-12 in-frame, single-gene knockout mutants: The Keio collection. *Mol. Syst. Biol*. **2**, 0008 (2006).
51. S. Bolte, F. P. Cordelieres, A guided tour into subcellular colocalization analysis in light microscopy. *J. Microsc.* **224**, 213–232 (2006).
52. A. J. M. Wollman, M. C. Leake, Millisecond single-molecule localization microscopy combined with convolution analysis and automated image segmentation to determine protein concentrations in complexly structured, functional cells, one cell at a time. *Faraday Discuss*. **184**, 401–424 (2015).
53. H. Miller, Z. Zhou, A. J. M. Wollman, M. C. Leake, Superresolution imaging of single DNA molecules using stochastic photoblinking of minor groove and intercalating dyes. *Methods* **88**, 81–88 (2015).
54. M. C. Leake, Analytical tools for single-molecule fluorescence imaging in cellulo. *Phys. Chem. Chem. Phys.* **16**, 12635–12647 (2014).
55. T. Bickel, A note on confined diffusion. *Phys. A* **377**, 24–32 (2007).
56. T. Kalwarczyk, M. Tabaka, R. Holyst, Biologistics-diffusion coefficients for complete proteome of *Escherichia coli*. *Bioinformatics* **28**, 2971–2978 (2012).
57. T. Lenn, M. C. Leake, Experimental approaches for addressing fundamental biological questions in living, functioning cells with single molecule precision. *Open Biol.* **2**, 120090 (2012).
58. M. C. Leake, D. Wilson, B. Bullard, R. M. Simmons, The elasticity of single kettin molecules using a two-bead laser-tweezers assay. *FEBS Lett.* **535**, 55–60 (2003).
59. A. P. J. Jansen, *An Introduction to Kinetic Monte Carlo Simulations of Surface Reactions* (Springer-Verlag, ed. 1, 2012).
60. M. Saito, M. Mastumoto, SIMD-oriented Fast Mersenne Twister: A 128-bit pseudorandom number generator, in *Monte Carlo and Quasi-Monte Carlo Methods* (Springer, 2008), pp. 607–622.
61. P. Cherepanov, W. Wackernagel, Gene disruption in *Escherichia coli*: Tc^R and Km^R Cassettes with the option of Flp-catalyzed excision of the antibiotic-resistance determinant. *Gene* **158**, 9–14 (1995).